Monthly Notices of the ROYAL ASTRONOMICAL SOCIETY

MNRAS **464,** 572–585 (2017) doi:10.1093/mnras/stw2354
Advance Access publication 2016 September 15

On the relationship between circumstellar disc size and X-ray outbursts in Be/X-ray binaries

I. M. Monageng,[1,2]★ V. A. McBride,[1,2] M. J. Coe,[3] I. A. Steele[4] and P. Reig[5,6]

[1]*South African Astronomical Observatory, P.O Box 9, Observatory, 7935 Cape Town, South Africa*
[2]*Department of Astronomy, University of Cape Town, Private Bag X3, 7701 Rondebosch, South Africa*
[3]*School of Physics and Astronomy, University of Southampton, Highfield, Southampton SO17 1BJ, UK*
[4]*Astrophysics Research Institute, Liverpool John Moores University, L3 5RF, Brownlow Hill, Liverpool, UK*
[5]*IESL, Foundation for Research and Technology-Hellas, GR-711 10 Heraklion, Crete, Greece*
[6]*Department of Physics and Institute of Theoretical Computational Physics, University of Crete, PO Box 2208, GR-710 03 Heraklion, Crete, Greece*

Accepted 2016 September 14. Received 2016 September 13; in original form 2016 July 25

ABSTRACT

We present long-term Hα monitoring results of five Be/X-ray binaries to study the Be disc size variations and their influence on type II (giant) X-ray outbursts. The work is done in the context of the viscous decretion disc model which predicts that Be discs in binary systems are truncated by resonant torques induced by the neutron star in its orbit. Our observations show that type II outbursts are not correlated (nor anticorrelated) with the disc size, as they are seen to occur both at relatively small and large Be disc radii. We discuss these observations in context of alternate interpretation of Be disc behaviour, such as precession, elongation and density effects, and with cognisance of the limitations of our disc size estimates.

Key words: stars: emission line, Be – X-rays: binaries.

1 INTRODUCTION

Be/X-ray binaries (BeXBs) are binary stellar systems which make up the largest subclass of the high-mass X-ray binary (HMXB) population (about two-thirds of the identified systems; Paul & Naik 2011). These systems are primarily composed of a massive, early-type donor (an Oe or Be star) and a neutron star (NS) accretor. The rapidly rotating Oe/Be primary is surrounded by a geometrically thin, Keplerian circumstellar disc in the equatorial regions. The presence and variations of the disc are detected observationally through infrared excess and Balmer emission lines in the optical spectra, the strongest and best studied of these being the Hα emission line (Porter & Rivinius 2003). The neutron star is generally in an eccentric orbit ($e \geq 0.3$) around the massive companion and a correlation in the $P_{\rm orb} - P_{\rm spin}$ diagram is observed, across a wide range of orbital periods ($24.3 \leq P_{\rm orb} \leq 262.6$ d; Corbet 1984, 1986). The interaction of the neutron star with the material in the circumstellar disc results in transient X-ray behaviour. The transient nature of BeXBs is characterized by two types of outburst events (Stella, White & Rosner 1986):

(1) Type I (normal outbursts), which have moderate luminosities ($L \leq 10^{37}$erg s^{-1}) and occur regularly, separated by the orbital period.

(2) Type II (giant outbursts), which display larger luminosities ($L \geq 10^{37}$erg s^{-1}). They are less frequent and are not modulated on the orbital period.

The extent to which the circumstellar disc grows is restricted by the neutron star in its orbit. The viscous decretion disc model explains how circumstellar discs interact with the neutron star, resulting in disc truncation (Lee, Osaki & Saio 1991; Okazaki & Negueruela 2001). Angular momentum is added to the inner regions of the disc by the Be star and the material is then transported to the outer parts via viscosity (Shakura–Sunyaev α-prescription for viscous stress is applied; Shakura & Sunyaev 1973). The disc is truncated at particular radii, where the ratio between the angular frequency of the disc rotation and that of the orbit is an integer. In BeXBs, the maximum observed Hα equivalent width correlates with the orbital period (Reig, Fabregat & Coe 1997; Reig et al. 2016), and this is interpreted as evidence for truncation of the circumstellar disc at a radius resonant with the neutron star orbit. This truncation is an expected outcome of the viscous disc model (Lee et al. 1991; Okazaki et al. 2002) and its effect on mass transfer has been explored by Negueruela & Okazaki (2001) and Negueruela et al. (2001). Except for this tidal truncation, the neutron star, being much less massive than the Be star, has very little effect on the circumstellar disc. However, when the circumstellar disc is truncated at a radius close to the inner Lagrangian point at periastron mass transfer to the neutron star can occur, resulting in an X-ray outburst (see fig. 6 in Negueruela & Okazaki 2001 for an illustration of the geometry).

This truncation suggests that the inner parts of Be star discs may be vertically thicker and/or denser than those of their isolated Be star

★ E-mail: itu@saao.ac.za

counterparts, while the outer disc density drops much more rapidly (Okazaki et al. 2002). While the physical extent of a Be star disc is very difficult to determine, the Hα emission line in Be stars is often used to provide an estimate. The Balmer lines are optically thick and produced through recombination. They are also formed in a large part of the disc, giving a much better idea of the physical extent than some of the helium or metal lines which are formed closer to the central star. Balmer line equivalent widths have been shown to correlate with estimates from optical interferometry (Grundstrom & Gies 2006). Huang (1972) shows that the peak separation in double-peaked emission lines resulting from a disc can be used to gauge the size of an emitting region, providing reliable sizes in the case of optically thin discs (Hummel 1994). Interferometric measurements suggest that disc emitting areas in the various bands are as large as a few tens of stellar radii, with disc sizes larger in the K band – in rough agreement with the dynamic estimates from Huang (Gies et al. 2007).

Silaj et al. (2010) show the dependence of Be star line profiles and equivalent widths on inclination angles, density and different power-law indices of the radial density dependence. In these models the Hα equivalent width correlates inversely with the peak separation, meaning both of these parameters are sensitive to changes in the disc size and/or density.

While the work of Grundstrom & Gies (2006) and Silaj et al. (2010) pertains to isolated Be stars, it is not clear how this translates to a case where the disc is truncated. Zamanov et al. (2001) show a rough inverse correlation between Hα equivalent width and peak separation for Be stars in BeXBs, and this seems to suggest that the situation is not so different in the case of the truncated disc. However, a degeneracy between the disc density and disc radius appears to persist.

Our goal in this paper is to investigate how the circumstellar disc size variations, through studying different properties of the Hα emission line, influence X-ray outbursts in BeXBs in the context of the viscous decretion disc model. The objects under study are Galactic Be/X-ray transients 1A 0535+262, 4U 0115+634, V 0332+53, EXO 2030+375 and 1A 1118−61.

The article is structured as follows: in Section 2 we present the observations and analysis of the data, while our method of estimating the circumstellar disc radius is addressed in Section 3. The results are presented in Section 4 and implications of the results are discussed in Section 5.

2 OBSERVATIONS

2.1 Optical observations

As part of a long-term monitoring programme of Galactic BeXBs, we have collected optical spectra between 2009 January 1 and 2013 July 21 with the Liverpool Telescope (LT; Steele 2001) and the Southern African Large Telescope (SALT; Buckley et al. 2006). These are supplemented with data from a number of other telescopes: 1.0-m Jacobus Kapteyn Telescope (La Palma), 2.5-m Isaac Newton Telescope (La Palma), 1.3-m Skinakas Telescope (Crete), 4.2-m William Herschel Telescope (La Palma), South African Astronomical Observatory 1.9-m telescope (South Africa).

For the SALT observations the Robert Stobie Spectrograph was used in longslit mode. The PG2300 grating (lines ruled at 2300 l mm^{-1}) was used with a wavelength coverage $\lambda\lambda$6200−7000 Å at exposure times of 180 s. A slit width of 1.5 arcsec was used for the observations, with a resolution of ∼1.6 Å and a resulting dispersion of 0.27 Å pixel^{-1}. Wavelength calibration of SALT data was performed by fitting lines in the observed arc with those of reference SALT spectra using a Neon lamp. The data reduction process of the semireduced SALT data (SALT pipeline performs overscan correction, bias subtraction, gain correction and corrections for amplifier cross-talk; Crawford et al. 2012) was undertaken with version 2.15.1 of IRAF.[1] Flux calibration was not applied, since the aim of obtaining the spectra was to measure EW(H α) of emission lines as well as to locate the peaks of double-peaked Hα emission lines.

On the LT the Fibre-fed Robotic Dual-beam Optical Spectrograph (FRODOSpec) integral field unit spectrograph was used in conjunction with the red Volume Phase Holographic grating. This covered a wavelength range $\lambda\lambda$5900–8000 Å at exposure times of 200 s (1A 0535+262) and 600 s (4U 0115+63 and V 0332+53), resulting in a central resolution of 1.3 Å and a dispersion of 0.6 Å pixel^{-1}. The reduction of raw data obtained with FRODOSpec was performed through a fully autonomous pipeline (Barnsley, Smith & Steele 2012). This comprised fibre tramline map generation, extraction of flux, arc fitting, sky subtraction and throughput correction.

1A 0535+262, 4U 0115+634 and V 0332+53 were also observed from the 1.3-m telescope of the Skinakas observatory located in the island of Crete (Greece). The spectra were obtained between the period 1999 and 2013. The telescope was equipped with a 2000 × 800 15 μm square pixel ISA SITe CCD and a 1302 l mm^{-1} grating, giving a nominal dispersion of 1.04 Å pixel^{-1} and a field of view of 19.6 arcmin × 7.8 arcmin.

Spectra were also obtained from the Anglo Australian, Jacobus Kapteyn, Isaac Newton and William Herschel telescopes and the South African Astronomical Observatory. Details of these data and their reductions have been previously published in Haigh, Coe & Fabregat (2004) and Coe et al. (2007).

The equivalent width and peak separation measurements utilized in this work are presented in Appendix A.

2.2 X-ray data

X-ray light curves from the *Rossi X-ray Timing Explorer* (*RXTE*) All Sky Monitor (ASM) and the *Swift* Burst Alert Telescope (BAT) Hard X-ray monitor have been used alongside the optical data as a tracer of the outburst and quiescent behaviour in the sources under study.

RXTE was active between 1995 December and 2012 January. The ASM (Levine et al. 1996) aboard *RXTE* scanned approximately 80 per cent of the sky every 90 min. The ASM light curves used in this work were downloaded from the archive[2] and comprised one-day averages of the source count rate in the 2–10 keV energy band.

Since 2004, the launch date of the *Swift* observatory, we also use X-ray light curves from the BAT (Barthelmy et al. 2005). The BAT observes 88 per cent of the sky every day, and the daily average light curves in the 15–50 keV band are available through the webpages of the *Swift*/BAT Hard X-ray transient monitor[3] (Krimm et al. 2013).

We perform a multiplicative conversion of the BAT count rates to equivalent ASM count rates by using the overlapping data (i.e. from 2004 to 2012). The scaling has been done so that outbursts and base flux levels match in these instruments. These light curves are plotted in units of luminosity in 2–10 keV band in the lower panels

[1] Image Reduction and Analysis Facility: iraf.noao.edu.
[2] http://xte.mit.edu/ASM_lc.html
[3] http://swift.gsfc.nasa.gov/results/transients/

Table 1. BeXBs and their parameters. $v \sin i$ is the projected rotational velocity of the donor star, M_* is the mass of the donor star, i is the estimated inclination of the orbit to the plane of the sky, $P_{\rm orb}$ is the orbital period and e the orbital eccentricity. The mean V-band magnitude is provided in the last column.

Object	$v \sin i$ (km s^{-1})[a]	M_* (M$_\odot$)[b]	i[c]	$P_{\rm orb}$(d)	e[d]	d(kpc)[e]	V mag[f]
1A 0535+262	254	20	27°	111.1	0.47	∼2	9.39
4U 0115+63	365	18	43°	24.32	0.34	7.8	15.19
V 0332+53	145	20	10.3°	34.67	0.37	∼7	15.13
EXO 2030+375	295	23	56°	46.02	0.416	∼5	19.7
1A 1118−61	300	18	25°	24.00	0.0	5	12.12

[a]Clark et al. (1998), Hutchings & Crampton (1981), Janot-Pacheco, Motch & Pakull (1988), Negueruela & Okazaki (2001), Janot-Pacheco, Ilovaisky & Chevalier (1981); [b]Negueruela & Okazaki (2001), Negueruela & Okazaki (2001), Motch et al. (1988); [c]Coe et al. (2006), Negueruela & Okazaki (2001), Coe et al. (1987), Reig et al. (1998), Okazaki & Negueruela (2001); [d]Finger et al. (1994); [e]Steele et al. (1998), Negueruela & Okazaki (2001), Negueruela et al. (1999), Parmar et al. (1989), Janot-Pacheco et al. (1981); [f]Reed (2003).

of the figures in Section 4. The distances used for the luminosities are presented in Table 1. This is not a rigorous scaling (which would account for the X-ray spectrum across the energy range) but it allows us to distinguish type I and type II outbursts.

There are no easily accessible X-ray light curves for epochs prior to 1995. X-ray all sky monitoring was possible between 1991 and 1998 through Burst and Transient Source Experiment (BATSE) on *Compton Gamma-Ray Observatory (CGRO)*, and through the Ariel ASM between 1974 and 1980. So for epochs prior to 1995 December, no X-ray light curves are shown, but type II outbursts as reported in the literature are indicated as vertical lines on the figures.

3 CIRCUMSTELLAR DISC RADIUS

Huang (1972) demonstrated that the size of the Hα emitting region of the circumstellar disc can be estimated by using the peak separation, ΔV, of the double peaked Hα emission lines if Keplerian velocity distribution of matter in the disc is assumed. We start from Newton's form of Kepler's third law, and taking peak separation of the double peaked Hα emission line as given by $\Delta V = 2v_{\rm pv}$, where $v_{\rm pv}$ is the projected velocity at the outer edge of the Hα emitting part of the disc. Taking into consideration the geometry of the disc with respect to our line of sight, the true velocity of the disc is then given by $v_{\rm tr} = v_{\rm pv}/\sin i$, where i is the inclination angle of the disc. The true velocity of the disc can therefore be expressed by $v_{\rm tr} = \Delta V/2\sin i$. Assuming that the orbits of particles in the disc are circular, with the prevailing force being the gravity of the Be star, the radius of the Hα emitting region of the disc can be given by

$$r = \frac{GM_* \sin^2 i}{(0.5\Delta V)^2}. \quad (1)$$

For single-peaked profiles the peak separation, ΔV, cannot be measured directly. However, Hanuschik (1989) demonstrated that there exists a linear relationship between ΔV EW and EW(Hα):

$$\log\left(\frac{\Delta V}{2v\sin i}\right) = -a\log\left(\frac{-\mathrm{EW}}{\text{Å}}\right) + b. \quad (2)$$

From a fit to the $\log(\frac{\Delta V}{2v\sin i})$ versus $\log(\frac{-\mathrm{EW}}{\text{Å}})$ plot for double-peaked line profiles, the values of the constants a and b can be obtained from the slope and intercept, respectively. So for emission lines which display single-peaked profiles, the disc radius could be estimated using measurements of the EW(Hα). Zamanov et al. (2001) derived parameters a and b for a sample of stars in a comparison study between circumstellar discs in BeXBs and isolated Be stars. This method of disc size estimation was applied to 1A 0535+262 (Coe et al. 2006) and more recently to HMXBs LSI+61°303, MWC 148 and MWC 656 (Zamanov et al. 2016).

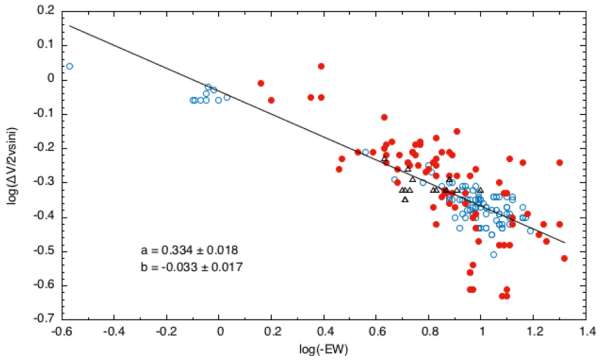

Figure 1. A plot of peak separation and EW(Hα) measurements of 1A 0535+262 (cyan circles), 4U 0115+634 (red circles) and V 0332+53 (triangles). The best-fitting line is overplotted, with fit parameters, a and b.

In our sample of BeXBs, only 1A 0535+262, 4U 0115+634 and V 0332+53 showed double-peaked Hα during some observations. Table 1 lists the parameters M_*, $v \sin i$ and i obtained from literature, and the fit for these sources is shown in Fig. 1.

The errors in the radius calculations were propagated from the errors in ΔV and EW(Hα). The typical error of a radius estimate obtained from direct measurements of ΔV (i.e. double-peaked Hα lines) has a range 10–15 per cent. For single-peaked profiles, the radius error bars display a larger range of 50–70 per cent the radius value – mainly due to the large scatter in the plot of $\log(\frac{\Delta V}{2v\sin i})$ versus $\log(\frac{-\mathrm{EW}}{\text{Å}})$, Fig. 1. The indirect estimates of ΔV (from inference using the relationship between ΔV and EW(Hα)) were checked with the double-peaked Hα profiles and the two methods give radius estimates that agree within error bars.

4 RESULTS

4.1 1A 0535+262

1A 0535+262 is one of the best-studied X-ray binary transients, discovered by *Ariel* V during a type II outburst (Rosenberg et al. 1975). The system consists of an O9.7IIIe primary star (Giangrande et al. 1980; Steele et al. 1998) and an X-ray pulsar in orbit around the primary. 1A 0535+262 is at a distance ∼2 kpc (Steele et al. 1998). Orbital measurements of the binary system reveal an orbital period of ∼111.1 d (Finger et al. 1994, 2006), an eccentricity of ∼0.47 (Finger et al. 1994) and pulse period of 103.39 s (Caballero et al. 2007).

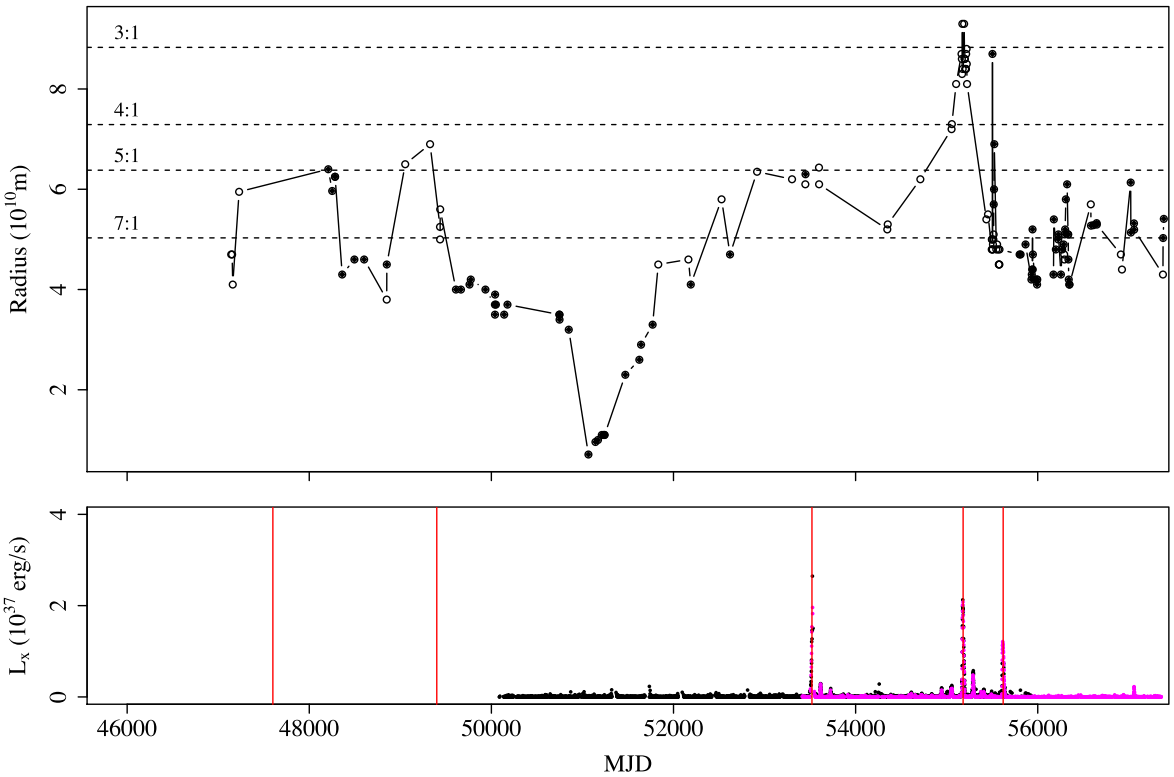

Figure 2. Top panel: evolution of the Be disc in 1A 0535+262. The size of the 3:1 r_{res}, 4:1 r_{res}, 5:1 r_{res} and 7:1 r_{res} are indicated in the plot. The filled circles indicate the radius calculations from double-peaked profiles of Hα and open circles represent single-peaked profiles. Lower panel: long-term X-ray light curve from the *RXTE* ASM and *Swift* BAT. The vertical lines in this panel show the peak times of type II X-ray outbursts.

During a period when there were no recorded X-ray outbursts (∼MJD 47140–∼MJD 47232, Fig. 2), the disc radius was below the 5:1 r_{res}, with radii ranging from $r \sim 4.1 \times 10^{10}$ m to $r \sim 6.2 \times 10^{10}$ m. 1A 0535+262 underwent a type II outburst which peaked at ∼MJD 47600 (March 1989; Giovannelli & Graziati 1992) for which there was no optical coverage of the system. Between MJD 48209 and MJD 49054 the disc displayed sizes below the 4:1 r_{res} ranging from $r \sim 3.8 \times 10^{10}$ m to $r \sim 6.7 \times 10^{10}$ m unaccompanied by X-ray activity (BATSE all sky monitoring started around MJD 48350). A type II outburst was then observed, peaking at ∼MJD 49400 and lasted for ∼50 d with a peak flux of ∼8 Crab at 20–50 keV (Bildsten et al. 1997). During this period the disc size was still below the 4:1 r_{res}, with a maximum radius of $r \sim 6.9 \times 10^{10}$ m (MJD 49327).

The disc appeared to have reached stability, with truncation at the 7:1 r_{res} for almost 3.5 yr (∼MJD 49611–∼MJD 50850) before going through a disc-loss phase as evidence by Hα in absorption (MJD 51055). A similar trend in the disc size was found by Grundstrom et al. (2007) in their study of 1A 0535+262 at this epoch. 1A 0535+262 underwent its first outburst after a 10 yr period of quiescence which peaked at ∼MJD 53500 (2005 May/June) and reached a flux of 4.5 Crab at 30 keV (Smith et al. 2005), followed by two type I outbursts. A series of type I outbursts starting at ∼MJD 54610. The fourth of these was unusual in that it was double peaked, with the first peak occurring ∼14 d before periastron passage and the second peak around periastron passage, at ∼MJD 55058.

At the start of the LT monitoring programme (MJD 55163) the disc radius as inferred from Hα measurements was close to 3:1 r_{res} ($r \sim 8.7 \times 10^{10}$ m). During this period 1A 0535+262 was already undergoing a type II outburst which peaked at ∼MJD 55180 with a peak flux of ∼5.14 Crab at 15–50 keV (Caballero et al. 2010). Following was a series of type I outbursts, the second of which was peculiar in that it was double peaked. The disc size had declined to truncation below the 5:1 r_{res} at ∼MJD 55436, while 1A 0535+262 underwent another type II outburst in 2011 February (peaking at ∼MJD 55620). 1A 0535+262 has since been in quiescence following the type II outburst in 2011 with the disc truncated below the 5:1 r_{res}.

4.2 4U 0115+63

4U 0115+63 is another well-studied BeXB transient. The system was initially reported as a discovery by the *Uhuru* satellite during its 1971 type II outburst (Giacconi et al. 1972; Forman et al. 1978). However, it was later noticed, after going through the *VELA* 5B archival data that it had already been detected in 1969 (Whitlock, Roussel-Dupre & Priedhorsky 1989). The optical companion in the binary system is a B0.2Ve star at a distance of 7.8 kpc (Negueruela & Okazaki 2001). Using the BATSE monitoring data of a sample of accreting pulsars, Bildsten et al. (1997) derived the orbital parameters: $P_{orb} = 24.317\,037(2)$ d, $a_X \sin i = 140.13(8)$ lt-s, $e = 0.3402(2)$, $T_{peri} =$ MJD 49279.2677(34). The pulse period of the pulsar is 3.614 690(2) s (Tamura et al. 1992). The type I outbursts in 4U 0115+63 are well explained in context of the truncated viscous decretion disc model and the particular orbital geometry of this source, while the semiregular type II outbursts are speculated to occur due to a warped, precessing circumstellar disc (Negueruela et al. 2001).

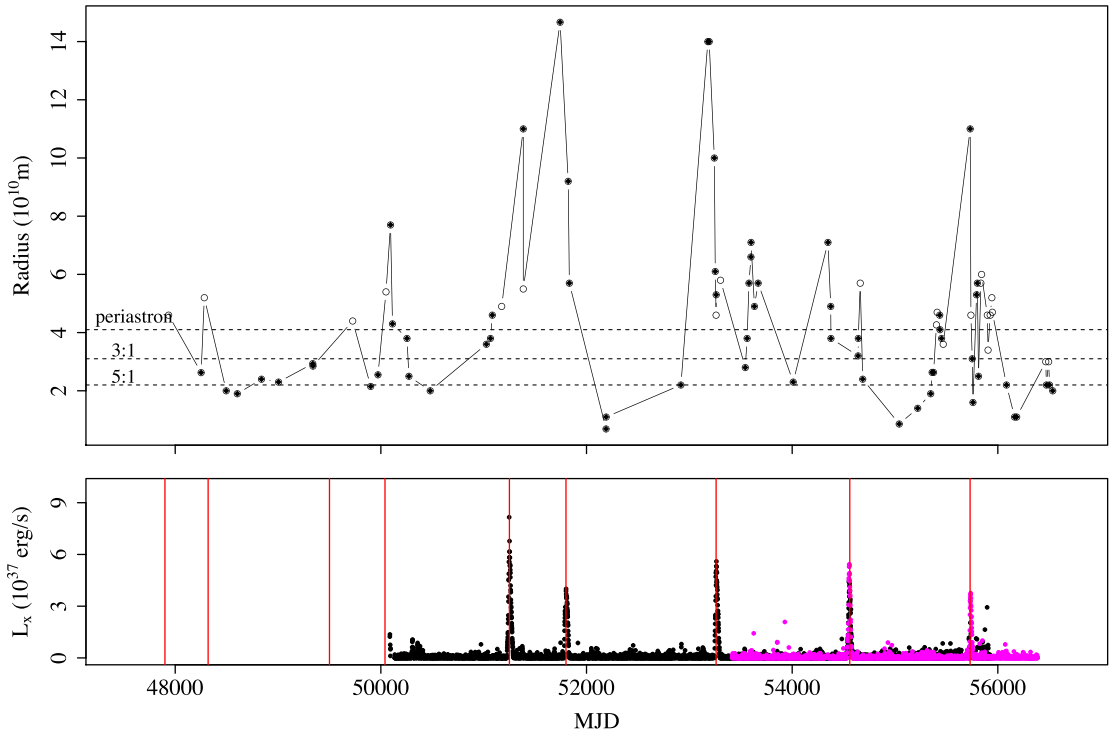

Figure 3. Top panel: evolution of the Be disc in 4U 0115+63. The sizes of the 3:1 $r_{\rm res}$, 5:1 $r_{\rm res}$ and periastron distance of the neutron star are indicated in the plot. The filled circles indicate the radius calculations from double-peaked profiles of Hα and open circles represent single-peaked profiles. Lower panel: long-term X-ray light curve from the *RXTE* ASM and *Swift* BAT. The vertical lines in this panel show the peak times of type II X-ray outbursts.

For the earliest measurements (∼MJD 47936, Fig. 3), the disc radius was comparable to periastron passage of the NS. During this period 4U 0115+63 underwent a type II outbursts in 1990 February (∼MJD 47900; Tamura et al. 1992). In 1991 March (∼MJD 48320), the system underwent another type II outburst (Cominsky, Roberts & Finger 1994), with the radius just above periastron passage a month before the peak of the outburst. A type II outburst was again observed in 1994 May/June (∼MJD 49500; Negueruela et al. 1997) with no optical coverage. Following this the disc appeared to have undergone a disc-growth phase, reaching a maximum of $r \sim 7.7 \times 10^{10}$ m at ∼MJD 50094 and then declining to a radius below near the 5:1 $r_{\rm res}$ (∼MJD 50480). A type II outburst, coinciding with this growth phase, was observed in 1995 November/December (peaking at ∼MJD 50040) with a peak flux of 0.7 Crab at 3–300 keV (Sazonov & Sunyaev 1995), as well as a rare series of type I outbursts separated by the orbital period (between MJD 50300 and MJD 50400) during the disc decline. Two type II outbursts were again observed, peaking at ∼MJD 51250 (1999 March) and ∼MJD 51750 (2000 August) when the apparent disc size reached values above periastron passage, up to $r \sim 1.5 \times 10^{11}$ m (∼MJD 51743). Following the 2000 August outburst, the disc underwent a low state, with radius values significantly below the 5:1 $r_{\rm res}$ (between $r \sim 7 \times 10^9$ m and $r \sim 2.2 \times 10^{10}$ m). The disc recovered to reach radii above periastron passage ($r \sim 1.4 \times 10^{10}$ m, ∼MJD 53180) on a time-scale of ∼260 d, accompanied by a type II outburst peaking at ∼MJD 53260. The disc decreased in size following the outburst but still above periastron passage, reaching radii up to $r \sim 7 \times 10^{10}$ m with no X-ray activity. 4U 0115+63 underwent a further type II outburst which peaked at ∼MJD 54560 for which there is no simultaneous optical coverage.

At the beginning of the LT monitoring of 4U 0115+63 (MJD 55220) the disc displayed sizes below the 5:1 $r_{\rm res}$, at $r \sim 1.4 \times 10^{10}$ m and grew to sizes larger than periastron passage, peaking at ∼MJD 55731 ($r \sim 1.1 \times 10^{11}$ m). A type II outburst was observed during disc-growth, peaking at ∼MJD 55730 (2011 May/June), which reached a flux of ∼0.8 Crab at energy band 3–300 keV (Boldin, Tsygankov & Lutovinov 2013). The disc has since returned to a low state, with sizes below the 3:1 $r_{\rm res}$ and has been in quiescence since the type II outburst in 2011 May/June.

4.3 V 0332+53

V 0332+53 is a transient X-ray pulsar which was discovered by *VELA* 5B during an outburst in 1973 (Terrell & Priedhorsky 1984). The optical companion of the system is an O8-9Ve star, BQ Cam (Negueruela et al. 1999), located at a distance ∼7 kpc. Using data from (*RXTE*) and *INTEGRAL* observations, Zhang et al. (2005) derived the following parameters: $P_{\rm spin} \approx 4.375$ s, $P_{\rm orb} = 34.67$ d, $e = 0.37$, $a_X \sin i \approx 86$ lt-s.

The apparent disc size in V 0332+53 has remained below the 5:1 $r_{\rm res}$ since the beginning of the optical monitoring. Prior to the commencement of the optical observations, V 0332+53 had already undergone a type II outburst which reached a peak flux of ∼0.3 Crab (2–20 keV) peaking at ∼MJD 47814 (Makishima et al. 1990). The system underwent two X-ray outburst events for which there is no simultaneous optical coverage: a type II outburst occurred between 2004 November and 2005 February (peaking at ∼MJD 53370) and a type I outburst which peaked at ∼MJD 54770.

The LT monitoring of V 0332+53 started when the system was undergoing a rare series of type I outbursts in 2009 (∼MJD 55160–

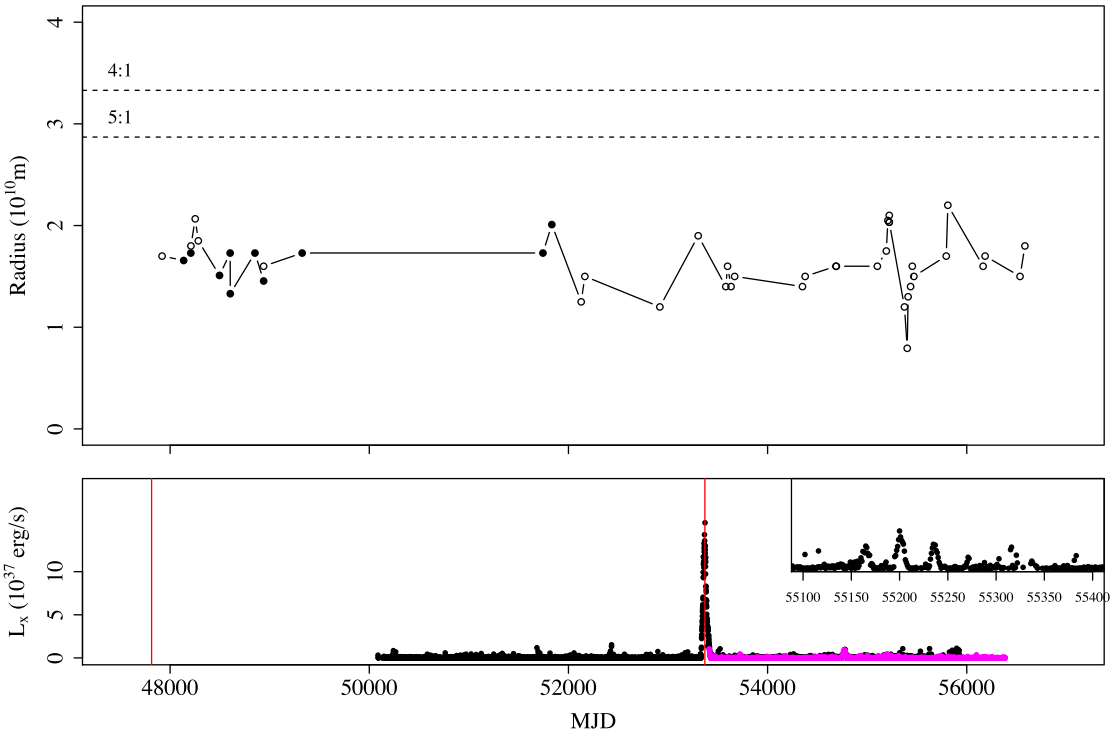

Figure 4. Top Panel: evolution of the Be disc in V 0332+53. The size of the 4:1 r_{res} and 5:1 r_{res} are indicated in the plots. The filled circles indicate the radius calculations from double-peaked profiles of Hα and open circles represent single-peaked profiles. Lower panel: long-term X-ray light curve from the *RXTE* ASM and *Swift* BAT. The vertical lines in this panel show the peak times of type II X-ray outbursts. The inset is a zoomed portion of the X-ray light curve illustrating the series of type I outbursts in 2009.

∼MJD 55320, see inset on Fig. 4). The disc was truncated below the 5:1 r_{res} during this period. V 0332+53 has been in quiescence since the end of the 2009 series of type I outbursts.

4.4 EXO 2030+375

EXO 2030+375 is an X-ray transient pulsar which was discovered with the *European X-ray Observatory Satellite* during a giant outburst in 1985 (MJD 46203; Parmar et al. 1989). The system is located at a distance of 5.3 kpc (Parmar et al. 1989). Optical and infrared studies of the system revealed the optical companion to be an early-type main-sequence star (B0Ve), with properties similar to those of V 0332+53 (Motch & Janot-Pacheco 1987; Coe et al. 1988). In the analysis of long-term *RXTE* data, Wilson, Fabregat & Coburn (2005) obtained orbital parameters: $P_{orb} = 46.0202(2)$ d, $e = 0.416(1)$, $a_X \sin i = 238(2)$ lt-s, $T_{peri} =$ JD 245 1099.93(2). The spin period of the pulsar is 41.4106(1) s (Naik et al. 2013).

Between MJD 48897 and MJD 49168 the radius of the Be disc in EXO 2030+375 showed a range of values all greater than the neutron star distance periastron, from $r \sim 1.5 \times 10^{11}$ m to r_{res}, at $r \sim 2.1 \times 10^{11}$ m (Fig. 5). The disc size had declined to $r \sim 1.2 \times 10^{11}$ m by MJD 50273. During this period EXO 2030+375 was displaying low intensity type I outbursts (Reig et al. 1998). The system underwent a rare type II outburst which peaked at ∼MJD 53950, with the disc size at $r \sim 1.2 \times 10^{11}$ m on the outburst decline but showing an increasing trend.

EXO 2030+375 is unusual among BeXBs in that it goes through long periods of type I outbursts that last for a few years. Other BeXBs, in contrast, undergo series of type I outbursts that usually last for a few orbits of the NS. The fact that the disc size is often larger than periastron distance could explain this (the NS interacts with the disc). This would support the idea that type I outbursts occur because the NS physically interacts with the disc at or near periastron. When the radius of the disc is smaller or of the order of periastron passage, X-ray activity decreases because the NS no longer passes through the disc.

4.5 1A 1118−61

1A 1118−61 is an X-ray transient which was discovered by the *Ariel-5* satellite in 1974 during a type II outburst (Eyles et al. 1975). The optical companion in the BeXB is an O9.5IV-Ve star at a distance 5 ± 2 kpc (Janot-Pacheco et al. 1981). In the analysis of data obtained with *RXTE/PCA*, Staubert et al. (2011) derived the orbital parameters: $P_{orb} = 24.0 \pm 0.4$ d, $a_X \sin i = 54.85 \pm 1.4$ lt-s, $e = 0.0$, $P_{spin} = 407.6546 \pm 0.0011$ s.

For the early measurements (MJD 49049–MJD 54226), the apparent disc size is larger than the orbital radius of the NS, with radii ranging between $r \sim 8.6 \times 10^{10}$ m and $r \sim 9.4 \times 10^{10}$ m. The two SALT data points are at $r \sim 8.8 \times 10^{10}$ m, below the orbital radius of the NS. The X-ray behaviour of 1A 1118−61 is characterized by long periods of quiescence and rare type II outbursts. The system underwent a type II outburst in 2009 (peaking at ∼MJD 54845) for which there was no optical coverage. Prior to this, 1A 1118−61 displayed one other outburst in 1992 January (MJD 48646; Coe et al. 1994) since its discovery in 1974. The very low luminosities of the type II outbursts ($<10^{37}$ erg s^{-1}) in Fig. 6 suggest that the object is probably less distant from us than the 5 kpc estimate (Janot-Pacheco et al. 1981) used in this work.

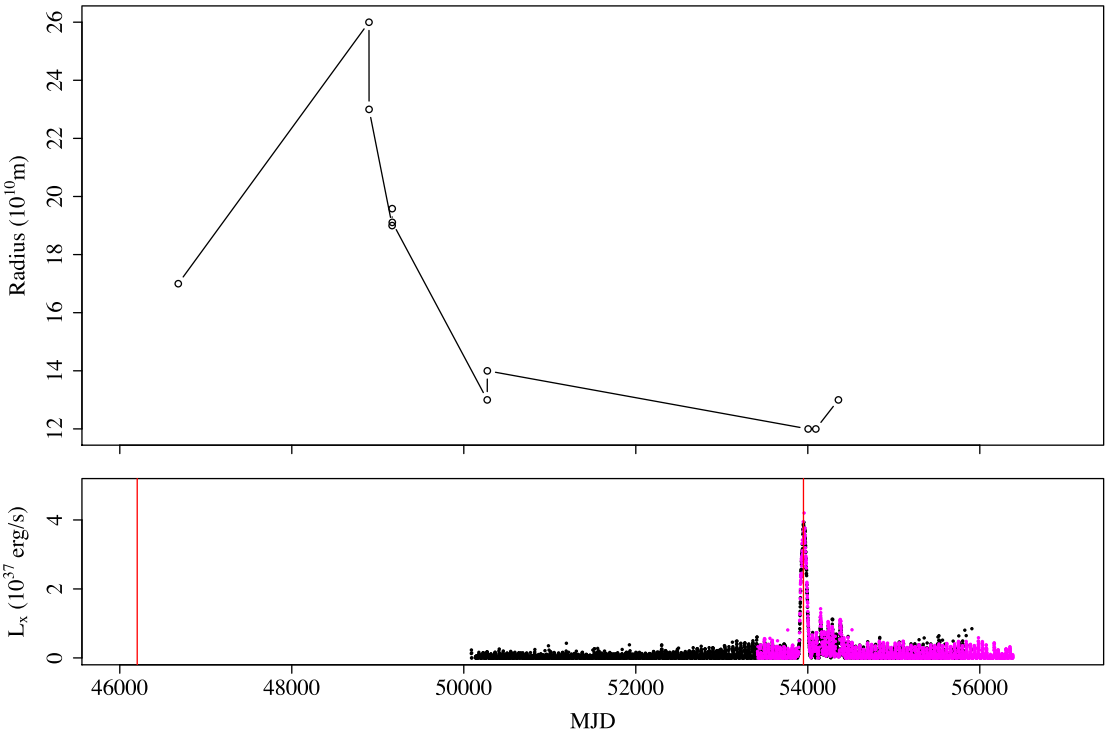

Figure 5. Top panel: evolution of the Be disc in EXO 2030+375. Lower panel: long-term X-ray light curve from the *RXTE* ASM and *Swift* BAT. The vertical lines in this panel show the peak times of type II X-ray outbursts. The vast number of type I outbursts is clearly visible throughout the X-ray light curve. The 5:1, 4:1, 3:1 resonance radii and periastron passage, not included in the plot on this scale, range between $r \sim 3.5 \times 10^{10}$m and $r \sim 6.1 \times 10^{10}$m.

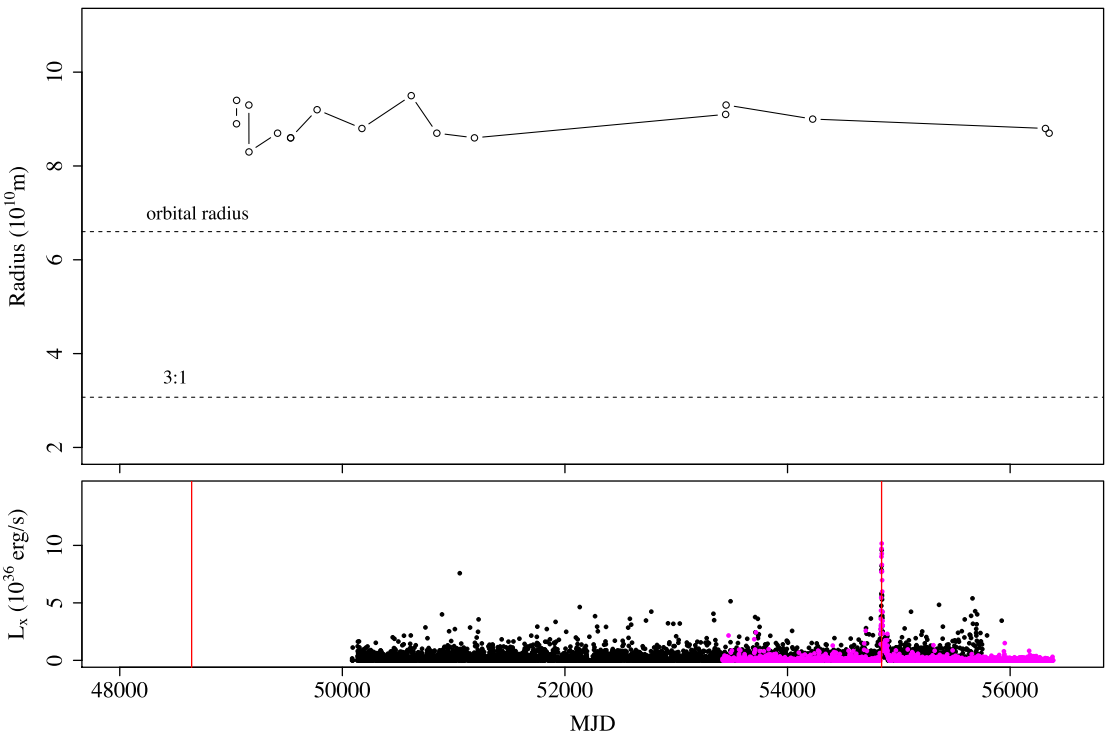

Figure 6. Top Panel: evolution of the Be disc in 1A 1118−61. The 3:1 resonance radius and the orbital radius of the neutron star are indicated. Lower panel: long-term X-ray light curve from the *RXTE* ASM and *Swift* BAT. The vertical lines in this panel show the peak times of type II X-ray outbursts.

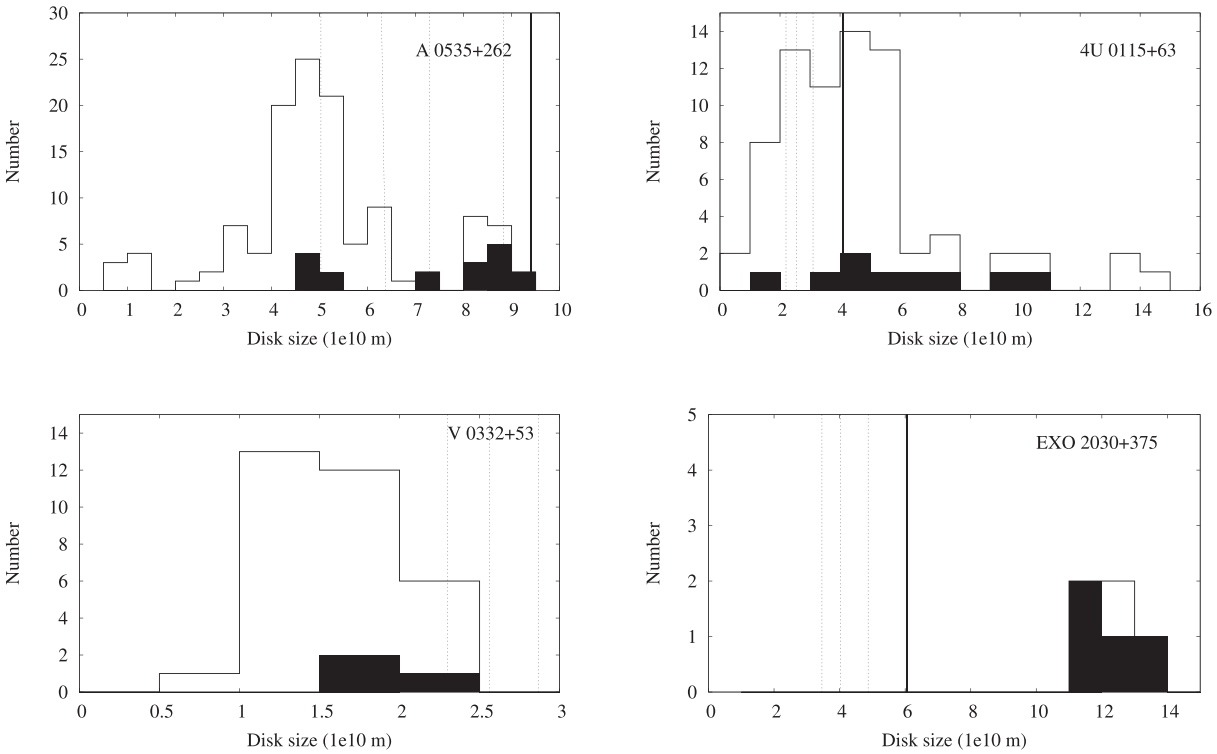

Figure 7. The distribution of disc sizes. Only Hα observations during the lifetime of the *RXTE*-ASM and *Swift* missions are shown. Measurements within 3 d of X-ray activity are highlighted in solid colour. Dotted lines show the 7:1, 5:1, 4:1 and 3:1 resonance radii (from small to large radii) for 1A 0535+262; 5:1, 4:1 and 3:1 resonance radii for 4U 0115+63; 7:1, 6:1 and 5:1 resonance radii for V 0332+53; 5:1, 4:1 and 3:1 resonance radii for EXO 2030+375, while the solid lines show the periastron distance of the neutron star.

5 DISCUSSION

Fig. 7 shows the data already presented as histograms of disc size. In these histograms, we only plot Hα disc size measurements for epochs that are covered by either the *RXTE* ASM or *Swift* hard X-ray monitoring (Krimm et al. 2013) data. Hα disc size estimates that occur within 3 d of a 5σ detection with either *RXTE* ASM or *Swift*-BAT are highlighted with solid colour histograms. 1A 1118−61 is not included as there no Hα measurements 'simultaneous' with X-ray activity. Looking at the evolution of the Be disc radius we are struck by a few interesting results which we discuss below.

5.1 Type II outbursts with small disc sizes

In a few instances, we see type II outbursts occurring around the time when the apparent disc size is smaller than the critical lobe radius[4] at periastron passage of the neutron star ($R_{\rm crit}$) in 1A 0535+262 and V 0332+53. During the 1994 (MJD 49500) type II outburst the disc size in 1A 0535+262 was below the 4:1 $r_{\rm res}$ (4:1 $r_{\rm res} \approx {\rm R_{crit}}$), while during the 2011 (MJD 53500) outburst in this system the disc was below the 5:1 $r_{\rm res}$. When the 2004 November type II outburst had already begun (MJD 53332) the disc in V0332+53 was still truncated below 5:1 $r_{\rm res}$ (3:1 $r_{\rm res} \approx {\rm R_{crit}}$), as well as approximately two cycles before the large intensity type I outburst in 2008 (MJD 55200). The apparent disc radius was still below the 5:1 $r_{\rm res}$ at the beginning of the LT monitoring while the system was undergoing a short series of type I outbursts.

[4] The critical lobe is the disc radius that reaches the L_1 point, i.e. mass transfer can occur when the disc is at, or larger than, the critical lobe.

In a very simple model, where the ΔV and EW(Hα) trace the disc radius, one would expect the disc to be large enough for material to be accreted to give rise to these outbursts. A number of possible reasons for the low Hα emission during the outbursts are discussed below.

5.1.1 *Precessing warped disc*

The Hα line profile shape is seen to undergo drastic changes which have been previously studied in 1A 0535+262 (Moritani et al. 2013) and 4U 0115+634 (Negueruela et al. 2001; Reig et al. 2007) and were interpreted to have resulted from a precessing warped disc. The low Hα emission during type II outbursts can be explained by a precessing warped disc, as was suggested to be the scenario for the 2011 outburst in 1A 0535+262 by Moritani et al. (2013). Here the changes in the Hα line profile were explained as arising from a warped region of the disc not being bright in Hα or hidden from the observer's line of sight (see their fig. 11).

5.1.2 *Elongated Be disc*

Strong disturbances of the Be disc resulting in elongation could explain low Hα emission during type II outbursts. An eccentric disc with the elongated region in the direction of the NS at periastron passage could result in type II outbursts. The low emission would be a line of sight effect: if the elongated region faces away from the observer, the observer is exposed to a smaller surface area of the disc, hence less Hα. In recent work, Martin et al. (2014) use 3D smoothed particle hydrodynamics simulations to suggest that type II outbursts result from a highly misaligned decretion disc ($i \geq 60^o$)

which is eccentric, allowing a large amount of matter to be accreted by the NS at close passage.

5.2 Type II outbursts with very large disc sizes

On a few occasions we see very large disc sizes for 1A 0535+262, 4U 0115+634 and EXO 2030+375 – larger than the expected truncation from the viscous decretion disc model. The apparent disc size in these systems sometimes reaches values above the periastron passage of the NS. It would be especially difficult for 4U 0115+634 and EXO 2030+375 to reach such large sizes since they have relatively small orbits and moderate eccentricities.

Moritani et al. (2013) suggested that a precessing warped disc during the 2009 outburst of 1A 0535+262 resulted in enhanced emission of Hα (see their fig. 11). Another possible cause for the large Hα emission, translating to large disc sizes, is an increase in disc-base density (Silaj et al. 2010). In this case the EW(Hα) increases without necessarily an increase in disc size.

5.3 Large disc sizes with no X-ray activity

The Be disc in 4U 0115+634 appeared to still have sizes above periastron passage at MJD 53562 with no X-ray activity approximately ∼250 d after the end of the type II outburst in 2004 (∼10 orbital cycles after the outburst). 1A 1118−61, although sparsely sampled in the optical, appears to show disc sizes consistently above the orbital radius of the NS, with unassociated X-ray activity. Again, increase in disc-base density as a result of a large accumulation of matter (not necessarily increase in radial extent) could explain the large emission with no X-ray activity.

5.4 Evidence for disc truncation

If truncation plays a dominant role in the size of the Be circumstellar disc, one expects the measurements of disc size to cluster at or below the truncation radii (the dotted lines in Fig. 7). Even in light of the uncertainties in the methodology and the degeneracy between disc size and disc density, there appears to be good evidence for this in both 1A 0535+262 (as discussed in Coe et al. 2006 and Grundstrom et al. 2007) and V 0332+53, and to a lesser extent in 4U 0115+63. The tendency for Be disc sizes in BeXBs to cluster around a specific level, from an observational viewpoint, has been discussed in literature (Grundstrom et al. 2007; Zamanov et al. 2013; Zamanov et al. 2016). In their fig. 4, Zamanov et al. (2016) show that, in the context of the viscous truncated disc model, the discs in gamma-ray binaries generally have sizes larger than the compact object periastron distance, similar to EXO 2030+375 and 1A 1118−61 in this study. The truncation of discs below periastron distance in BeXBs may be related to the transient X-ray behaviour in these systems, i.e. on occasions when the disc size reaches values near or greater than periastron distance, X-ray activity is observed. 1A 1118−61 and EXO 2030+375 do not show convincing evidence for truncation, despite the well-behaved periodic outbursts exhibited by EXO 2030+375. It is worth noting that the disc size estimates for both these objects are based on single-peaked profiles calibrated through the empirical relationship shown in Fig. 1. Measurements of the disc size based on single-peaked profiles have large uncertainties (Section 3) and are thus unreliable as indicators of disc truncation.

6 CONCLUSION

We have presented results from long-term spectroscopic monitoring of five BeXB systems to study the evolution of Be disc radius and look at its influence on X-ray outbursts, in the context of the viscous decretion disc model. The Hα emission line was used to obtain an estimate of the disc size and the main result is that type I outbursts generally occur when the Be disc radius is truncated at radii close to/larger than the critical lobe radius at periastron passage. This provides additional evidence (cf. Reig et al. 2016) for the viscous disc model. Type II outbursts, however, are difficult to predict solely based on disc size information, as these are seen to occur when the apparent disc size is large (larger than $R_{\rm crit}$), as well as when the disc is smaller than $R_{\rm crit}$.

As is becoming clear from other recent analyses of Hα data (Moritani et al. 2013) and disc simulations (Martin et al. 2014), the circumstellar disc behaviour is more complex than just growth, decay and truncation. The large disc sizes estimated on this assumption are unphysical and more complex behaviours such as warping, ellipticity or increases in the base density must be invoked to explain the observations presented here.

ACKNOWLEDGEMENTS

IM acknowledges funding from SKA, South Africa. VAM acknowledges funding from the NRF, South Africa and the World Universities Network.

REFERENCES

Barnsley R. M., Smith R. J., Steele I. A., 2012, Astron. Nachr., 333, 101
Barthelmy S. D. et al., 2005, Space Sci. Rev., 120, 143
Bildsten L. et al., 1997, ApJS, 113, 367
Boldin P. A., Tsygankov S. S., Lutovinov A. A., 2013, Astron. Lett., 39, 375
Buckley D. A. H., Charles P. A., Nordsieck K. H., O'Donoghue D., 2006, in Whitelock P., Dennefeld M., Leibundgut B., eds, Proc. IAU Symp. 232, The Scientific Requirements for Extremely Large Telescopes. Cambridge Univ. Press, Cambridge, p. 1
Caballero I. et al., 2007, A&A, 465, L21
Caballero I. et al., 2010, preprint (arXiv:1003.2969)
Clark J. S., Steele I. A., Coe M. J., Roche P., 1998, MNRAS, 297, 657
Coe M. J., Payne B. J., Hanson C. G., Longmore A. J., 1987, MNRAS, 226, 455
Coe M. J., Payne B. J., Longmore A., Hanson C. G., 1988, MNRAS, 232, 865
Coe M. J. et al., 1994, A&A, 289, 784
Coe M. J., Reig P., McBride V. A., Galache J. L., Fabregat J., 2006, MNRAS, 368, 447
Coe M. J. et al., 2007, MNRAS, 378, 1427
Cominsky L., Roberts M., Finger M. H., 1994, in Fichtel C. E., Gehrels N., Norris J. P., eds, AIP Conf. Proc. Vol. 304, The Second Compton Symposium. Am. Inst. Phys., New York, p. 294
Corbet R. H. D., 1984, A&A, 141, 91
Corbet R. H. D., 1986, MNRAS, 220, 1047
Crawford S. M. et al., 2012, Astrophysics Source Code Library, record ascl:1207.010
Eyles C. J., Rosenberg F. D., Skinner G. K., Willmore A. P., 1975, IAU Circ., 2752, 1
Finger M. H., Cominsky L. R., Wilson R. B., Harmon B. A., Fishman G. J., 1994, in Holt S., Day C. S., eds, AIP Conf. Proc. Vol. 308, The Evolution of X-ray Binaries. Am. Inst. Phys., New York, p. 459
Finger M. H., Camero-Arranz A., Kretschmar P., Wilson C., Patel S., 2006, in AAS/High Energy Astrophysics Division #9. p. 359
Forman W., Jones C., Cominsky L., Julien P., Murray S., Peters G., Tananbaum H., Giacconi R., 1978, ApJS, 38, 357
Giacconi R., Murray S., Gursky H., Kellogg E., Schreier E., Tananbaum H., 1972, ApJ, 178, 281
Giangrande A., Giovannelli F., Bartolini C., Guarnieri A., Piccioni A., 1980, A&AS, 40, 289

Gies D. R. et al., 2007, ApJ, 654, 527
Giovannelli F., Graziati L. S., 1992, Space Sci. Rev., 59, 1
Grundstrom E. D., Gies D. R., 2006, ApJ, 651, L53
Grundstrom E. D. et al., 2007, ApJ, 660, 1398
Haigh N. J., Coe M. J., Fabregat J., 2004, MNRAS, 350, 1457
Hanuschik R. W., 1989, Ap&SS, 161, 61
Huang S.-S., 1972, ApJ, 171, 549
Hummel W., 1994, A&A, 289, 458
Hutchings J. B., Crampton D., 1981, ApJ, 247, 222
Janot-Pacheco E., Ilovaisky S. A., Chevalier C., 1981, A&A, 99, 274
Janot-Pacheco E., Motch C., Pakull M. W., 1988, A&A, 202, 81
Krimm H. A. et al., 2013, ApJS, 209, 14
Lee U., Osaki Y., Saio H., 1991, MNRAS, 250, 432
Levine A. M., Bradt H., Cui W., Jernigan J. G., Morgan E. H., Remillard R., Shirey R. E., Smith D. A., 1996, ApJ, 469, L33
Makishima K. et al., 1990, ApJ, 365, L59
Martin R. G., Nixon C., Armitage P. J., Lubow S. H., Price D. J., 2014, ApJ, 790, L34
Moritani Y. et al., 2013, PASJ, 65, 83
Motch C., Janot-Pacheco E., 1987, A&A, 182, L55
Motch C., Pakull M. W., Janot-Pacheco E., Mouchet M., 1988, A&A, 201, 63
Naik S., Maitra C., Jaisawal G. K., Paul B., 2013, ApJ, 764, 158
Negueruela I. et al., 1997, MNRAS, 284, 859
Negueruela I., Okazaki A. T., 2001, A&A, 369, 108
Negueruela I., Roche P., Fabregat J., Coe M. J., 1999, MNRAS, 307, 695
Negueruela I., Okazaki A. T., Fabregat J., Coe M. J., Munari U., Tomov T., 2001, A&A, 369, 117
Okazaki A. T., Negueruela I., 2001, A&A, 377, 161
Okazaki A. T., Bate M. R., Ogilvie G. I., Pringle J. E., 2002, MNRAS, 337, 967
Parmar A. N., White N. E., Stella L., Izzo C., Ferri P., 1989, ApJ, 338, 359
Paul B., Naik S., 2011, Bull. Astron. Soc. India, 39, 429
Porter J. M., Rivinius T., 2003, PASP, 115, 1153
Reed B. C., 2003, AJ, 125, 2531
Reig P., Fabregat J., Coe M. J., 1997, A&A, 322, 193
Reig P., Stevens J. B., Coe M. J., Fabregat J., 1998, MNRAS, 301, 42
Reig P., Larionov V., Negueruela I., Arkharov A. A., Kudryavtseva N. A., 2007, A&A, 462, 1081
Reig P., Nersesian A., Zezas A., Gkouvelis L., Coe M. J., 2016, A&A, 590, A122
Rosenberg F. D., Eyles C. J., Skinner G. K., Willmore A. P., 1975, Nature, 256, 628
Sazonov S., Sunyaev R., 1995, IAU Circ., 6272, 2
Shakura N. I., Sunyaev R. A., 1973, A&A, 24, 337
Silaj J., Jones C. E., Tycner C., Sigut T. A. A., Smith A. D., 2010, ApJS, 187, 228
Smith D. M. et al., 2005, Astron. Telegram, 557, 1
Staubert R., Pottschmidt K., Doroshenko V., Wilms J., Suchy S., Rothschild R., Santangelo A., 2011, A&A, 527, A7
Steele I. A., 2001, Astron. Nachr., 322, 307
Steele I. A., Negueruela I., Coe M. J., Roche P., 1998, MNRAS, 297, L5
Stella L., White N. E., Rosner R., 1986, ApJ, 308, 669
Tamura K., Tsunemi H., Kitamoto S., Hayashida K., Nagase F., 1992, ApJ, 389, 676
Terrell J., Priedhorsky W. C., 1984, ApJ, 285, L15
Whitlock L., Roussel-Dupre D., Priedhorsky W., 1989, ApJ, 338, 381
Wilson C. A., Fabregat J., Coburn W., 2005, ApJ, 620, L99
Zamanov R. K., Reig P., Martí J., Coe M. J., Fabregat J., Tomov N. A., Valchev T., 2001, A&A, 367, 884
Zamanov R., Stoyanov K., Martí J., Tomov N. A., Belcheva G., Luque-Escamilla P. L., Latev G., 2013, A&A, 559, A87
Zamanov R. K., Stoyanov K. A., Marti J., Latev G. Y., Nikolov Y. M., Bode M. F., Luque-Escamilla P. L., 2016, A&A, 593, A97
Zhang S., Qu J.-L., Song L.-M., Torres D. F., 2005, ApJ, 630, L65

APPENDIX A: OPTICAL SPECTROSCOPIC DATA

The following are the Hα emission line parameters of the BeXBs in study. Columns 1 and 2 list the modified Julian dates and calculated radii, respectively. The measured peak separations and Hα equivalent widths are listed in columns 3 and 4, respectively. Column 5 lists the different telescopes used to obtain the spectra: Jacobus Kapetyn Telescope (JKT), Isaac Newton Telescope (INT), Skinakas Telescope (Ski), South African Astronomical Observatory 1.9-m telescope (SAAO), Russian-Turkish 1.5 m telescope (RT), Liverpool Telescope (LT), Southern African Large Telescope (SALT).

Table A1. 1A 0535+262: EW(Hα) and ΔV measurements.

MJD	Radius (m)	ΔV (km s^{-1})	EW(Hα) (Å)	Telescope
47143	5.01×10^{10}		-11.30 ± 0.65	INT
47143	4.40×10^{10}		-9.38 ± 0.57	INT
47153	4.65×10^{10}		-10.20 ± 0.73	INT
47160	4.06×10^{10}		-8.32 ± 0.89	INT
47230	6.17×10^{10}		-15.56 ± 0.91	INT
47230	5.73×10^{10}		-13.91 ± 0.23	INT
48209	6.70×10^{10}	180.2 ± 7.2	-11.05 ± 0.42	INT
48209	6.20×10^{10}	187.2 ± 9.4	-9.79 ± 0.30	INT
48209	6.30×10^{10}	187.1 ± 7.5	-9.81 ± 0.31	INT
48252	4.90×10^{10}		-11.02 ± 0.52	INT
48252	6.00×10^{10}	191.5 ± 13.4	-11.89 ± 0.96	INT
48252	5.90×10^{10}	191.9 ± 7.7	-11.63 ± 0.35	INT
48252	6.00×10^{10}	190.4 ± 9.5	-12.15 ± 0.46	INT
48283	6.30×10^{10}	186.9 ± 11.2	-10.43 ± 0.63	INT
48283	6.20×10^{10}	188.4 ± 7.7	-10.55 ± 0.44	INT
48284	6.30×10^{10}	186.9 ± 11.2	-9.89 ± 0.76	INT
48284	6.20×10^{10}	188.5 ± 13.2	-9.88 ± 0.87	INT
48362	4.30×10^{10}	225.5 ± 18.0	-7.52 ± 0.92	WHT
48362	4.30×10^{10}	225.5 ± 16.5	-7.52 ± 0.13	WHT
48496	4.60×10^{10}	218.3 ± 8.7	-9.57 ± 0.25	INT
48496	4.60×10^{10}	217.9 ± 9.8	-9.99 ± 0.70	INT
48603	4.60×10^{10}	217.1 ± 10.5	-12.69 ± 0.57	INT
48851	3.81×10^{10}		-7.55 ± 0.76	INT
48852	4.50×10^{10}	219.8 ± 15.4	-8.92 ± 0.50	INT
49054	6.53×10^{10}		-16.93 ± 0.98	INT
49327	6.93×10^{10}		-18.51 ± 1.11	INT
49436	4.89×10^{10}		-10.99 ± 0.45	JKT
49436	5.57×10^{10}		-13.35 ± 0.77	JKT
49437	5.01×10^{10}		-11.35 ± 0.86	JKT
49438	5.61×10^{10}		-13.48 ± 0.33	JKT
49611	4.00×10^{10}	233.1 ± 21.0	-11.59 ± 0.21	JKT
49666	4.00×10^{10}	234.3 ± 13.5	-11.66 ± 0.30	SAAO
49760	4.10×10^{10}	229.8 ± 13.8	-9.77 ± 0.45	JKT
49774	4.20×10^{10}	228.4 ± 11.4	-10.03 ± 0.50	SAAO
49935	4.00×10^{10}	235.2 ± 10.9	-9.68 ± 0.31	JKT
50039	3.70×10^{10}	242.6 ± 9.7	-9.39 ± 0.23	SAAO
50040	3.50×10^{10}	251.7 ± 10.0	-7.76 ± 1.23	SAAO
50041	3.60×10^{10}	246.8 ± 11.3	-8.50 ± 0.46	SAAO
50041	4.20×10^{10}	$228.7 \pm 13.$	-8.50 ± 0.98	SAAO
50050	3.70×10^{10}	242.5 ± 7.1	-8.42 ± 0.16	JKT
50141	3.50×10^{10}	248.8 ± 10.5	-9.66 ± 0.25	SAAO
50177	3.70×10^{10}	242.2 ± 12.2	-8.98 ± 0.51	SAAO
50747	3.50×10^{10}	250.6 ± 7.9	-7.08 ± 0.69	JKT
50748	3.50×10^{10}	250.8 ± 21.2	-8.79 ± 0.44	JKT
50749	3.40×10^{10}	251.9 ± 13.4	-7.52 ± 0.76	JKT
50850	3.20×10^{10}	259.6 ± 18.8	-4.64 ± 0.92	SAAO
51066	7.10×10^{09}	556.1 ± 16.0	-0.27 ± 0.21	Ski
51143	9.50×10^{09}	479.9 ± 9.0	-0.91 ± 0.20	INT

Table A1 *– continued*

MJD	Radius (m)	ΔV (km s^{-1})	EW(Hα) (Å)	Telescope
51143	9.70×10^{09}	475.0 ± 13.8	− 0.96 ± 0.25	INT
51171	1.00×10^{10}	464.5 ± 5.7	− 0.90 ± 0.31	WHT
51213	1.10×10^{10}	446.1 ± 9.5	− 0.80 ± 0.13	INT
51231	1.10×10^{10}	447.5 ± 15.3	− 1.00 ± 0.22	INT
51231	1.10×10^{10}	448.4 ± 7.9	− 1.06 ± 0.20	INT
51241	1.10×10^{10}	442.1 ± 12.1	− 0.82 ± 0.15	INT
51241	1.10×10^{10}	440.0 ± 13.2	− 0.90 ± 0.34	INT
51244	1.10×10^{10}	445.8 ± 18.2	− 0.85 ± 0.31	INT
51471	2.30×10^{10}	311.3 ± 11.0	− 3.66 ± 0.65	INT
51625	2.60×10^{10}	288.4 ± 4.8	− 6.31 ± 0.91	INT
51644	2.90×10^{10}	275.2 ± 19.4	− 6.48 ± 0.23	INT
51771	3.30×10^{10}	257.0 ± 9.4	− 6.00 ± 0.91	INT
51833	4.49×10^{10}		− 9.57 ± 0.34	Ski
51833	4.46×10^{10}		− 9.67 ± 0.56	Ski
52164	4.57×10^{10}		− 9.91 ± 0.11	Ski
52190	4.10×10^{10}	230.2 ± 19.6	− 11.14 ± 0.04	Ski
52190	4.10×10^{10}	230.3 ± 17.6	− 11.10 ± 0.12	Ski
52528	5.82×10^{10}		− 14.27 ± 0.90	Ski
52621	4.70×10^{10}	215.6 ± 11.6	− 14.50 ± 0.76	Ski
52918	4.93×10^{10}		− 11.12 ± 0.45	Ski
52918	7.77×10^{10}		− 21.96 ± 0.32	Ski
53302	6.23×10^{10}		− 15.79 ± 1.01	Ski
53448	6.11×10^{10}		− 15.33 ± 0.23	Ski
53450	6.30×10^{10}	186.3 ± 7.4	− 15.50 ± 0.91	Ski
53598	6.20×10^{10}		− 15.69 ± 0.22	Ski
53598	6.20×10^{10}		− 15.67 ± 0.46	Ski
53598	6.88×10^{10}		− 18.33 ± 0.89	Ski
53599	6.19×10^{10}		− 15.63 ± 0.70	Ski
53599	6.05×10^{10}		− 14.91 ± 0.57	Ski
53599	6.10×10^{10}		− 15.10 ± 0.99	Ski
53599	6.20×10^{10}		− 15.62 ± 0.34	Ski
54348	5.20×10^{10}		− 12.03 ± 0.78	Ski
54353	5.33×10^{10}		− 12.50 ± 0.50	Ski
54711	6.19×10^{10}		− 15.63 ± 0.34	Ski
55054	7.21×10^{10}		− 19.63 ± 0.56	Ski
55057	7.26×10^{10}		− 19.85 ± 0.68	Ski
55104	8.14×10^{10}		− 23.55 ± 0.91	Ski
55163.13	8.72×10^{10}		− 26.09 ± 0.92	LT
55167.01	8.57×10^{10}		− 25.43 ± 1.53	LT
55169.13	8.32×10^{10}		− 24.33 ± 0.43	LT
55172.13	9.29×10^{10}		− 28.70 ± 0.90	LT
55175.90	8.36×10^{10}		− 24.50 ± 0.54	LT
55191.89	9.33×10^{10}		− 28.89 ± 0.55	LT
55196.89	8.64×10^{10}		− 25.76 ± 0.90	LT
55199.86	8.65×10^{10}		− 25.78 ± 0.12	LT
55203.93	8.44×10^{10}		− 24.86 ± 0.45	LT
55208.91	8.43×10^{10}		− 24.82 ± 0.88	LT
55211.86	8.38×10^{10}		− 24.58 ± 0.97	LT
55214.13	8.72×10^{10}		− 26.13 ± 0.43	LT
55219.02	8.80×10^{10}		− 26.46 ± 0.65	LT
55220.89	8.51×10^{10}		− 25.16 ± 0.45	LT
55223.95	8.13×10^{10}		− 23.51 ± 0.71	LT
55436	5.45×10^{10}		− 12.92 ± 0.43	Ski
55454	5.50×10^{10}		− 13.11 ± 0.71	Ski
55495.12	4.83×10^{10}		− 10.80 ± 0.90	LT
55496.14	4.99×10^{10}		− 11.34 ± 0.42	LT
55499.23	4.99×10^{10}		− 11.22 ± 0.32	LT
55502.13	4.83×10^{10}		− 10.77 ± 0.67	LT
55503	8.70×10^{10}	158.6 ± 6.3	− 11.13 ± 0.90	Ski
55505.13	4.80×10^{10}		− 10.70 ± 0.55	LT
55508.24	4.94×10^{10}		− 11.17 ± 0.42	LT

Table A1 *– continued*

MJD	Radius (m)	ΔV (km s^{-1})	EW(Hα) (Å)	Telescope
55513.11	5.02×10^{10}		− 11.42 ± 0.55	LT
55516.02	5.14×10^{10}		− 11.82 ± 0.23	LT
55517.13	5.70×10^{10}	196.4 ± 10.1	− 11.58 ± 0.53	LT
55520.17	6.00×10^{10}	191.5 ± 6.7	− 11.82 ± 0.67	LT
55523.13	6.90×10^{10}	178.6 ± 10.4	− 10.94 ± 0.88	LT
55545.13	4.77×10^{10}		− 10.59 ± 0.70	LT
55554.18	4.94×10^{10}		− 11.16 ± 0.50	LT
55565.13	4.83×10^{10}		− 10.78 ± 0.34	LT
55572.88	4.49×10^{10}		− 9.65 ± 0.66	LT
55574.87	4.53×10^{10}		− 9.79 ± 0.21	LT
55578.94	4.52×10^{10}		− 9.75 ± 0.12	LT
55580.13	4.77×10^{10}		− 10.57 ± 0.37	LT
55801	4.70×10^{10}	215.2 ± 5.9	− 9.63 ± 0.31	Ski
55812	4.70×10^{10}	215.2 ± 12.1	− 9.30 ± 0.36	Ski
55866	4.90×10^{10}	210.5 ± 8.1	− 10.85 ± 0.63	Ski
55930.92	4.20×10^{10}	227.9 ± 8.2	− 9.04 ± 0.44	LT
55934.99	4.30×10^{10}	226.8 ± 9.0	− 10.02 ± 0.76	LT
55938.95	4.40×10^{10}	222.1 ± 5.5	− 10.34 ± 0.87	LT
55943.12	5.20×10^{10}	204.9 ± 9.4	− 10.47 ± 0.31	LT
55945.03	4.40×10^{10}	221.9 ± 11.4	− 9.88 ± 00.23	LT
55946.91	4.70×10^{10}	216.7 ± 8.7	− 10.41 ± 1.03	LT
55966.93	4.20×10^{10}	228.0 ± 9.1	− 9.72 ± 0.26	LT
55990.90	4.20×10^{10}	227.9 ± 9.0	− 8.31 ± 0.38	LT
55992.99	4.10×10^{10}	230.6 ± 9.2	− 7.61 ± 0.16	LT
55994.92	4.20×10^{10}	229.5 ± 11.5	− 7.81 ± 0.25	LT
56173.16	4.30×10^{10}	224.9 ± 9.0	− 8.87 ± 0.51	LT
56177.16	5.40×10^{10}	201.9 ± 12.1	− 8.81 ± 0.79	LT
56199.24	4.80×10^{10}	212.9 ± 8.5	− 9.00 ± 0.44	LT
56225.11	5.00×10^{10}	209.6 ± 10.5	− 9.03 ± 0.76	LT
56227.02	5.10×10^{10}	208.1 ± 14.6	− 9.38 ± 0.92	LT
56254.94	4.30×10^{10}	224.9 ± 9.0	− 9.66 ± 0.21	LT
56269.05	4.80×10^{10}	214.6 ± 8.6	− 10.58 ± 0.20	LT
56285.04	4.90×10^{10}	211.9 ± 12.7	− 11.46 ± 0.57	LT
56290.92	4.71×10^{10}		− 10.38 ± 0.75	LT
56292.96	4.65×10^{10}		− 10.18 ± 0.73	LT
56295.11	5.10×10^{10}	206.7 ± 8.3	− 11.84 ± 0.98	LT
56301	5.20×10^{10}	205.2 ± 9.0	− 11.71 ± 0.67	LT
56308.99	5.80×10^{10}	193.9 ± 7.8	− 12.78 ± 0.50	LT
56322.97	6.10×10^{10}	189.1 ± 13.2	− 12.04 ± 0.27	LT
56332.90	5.20×10^{10}	204.3 ± 12.2	− 12.75 ± 0.54	LT
56332.99	5.00×10^{10}	208.9 ± 10.5	− 12.65 ± 0.43	LT
56334.90	5.10×10^{10}	207.8 ± 8.3	− 12.91 ± 0.55	LT
56337.05	4.60×10^{10}	217.8 ± 10.9	− 12.64 ± 0.43	LT
56340.96	4.20×10^{10}	227.3 ± 9.1	− 13.06 ± 1.12	LT
56346.95	4.10×10^{10}	231.3 ± 12.7	− 12.55 ± 0.80	LT
56348.89	4.10×10^{10}	230.1 ± 13.8	− 13.32 ± 0.51	LT
56583	5.98×10^{10}		− 14.83 ± 0.67	Ski
56583.04	5.40×10^{10}		− 12.74 ± 0.78	LT
56585.05	5.28×10^{10}	203.7 ± 9.2	− 14.81 ± 0.98	LT
56611.17	5.28×10^{10}	203.5 ± 10.7	− 14.31 ± 0.54	LT
56647.07	5.33×10^{10}	202.7 ± 8.1	− 14.30 ± 0.34	LT
56649.13	5.30×10^{10}	203.3 ± 8.1	− 14.29 ± 0.68	LT
56913.12	4.68×10^{10}		− 10.30 ± 0.90	LT
56925.11	4.42×10^{10}		− 9.44 ± 0.21	LT
57020.96	6.14×10^{10}	188.9 ± 7.6	− 8.34 ± 0.33	LT
57022.99	5.14×10^{10}	206.4 ± 8.2	− 9.53 ± 0.44	LT
57057.09	5.32×10^{10}	202.8 ± 4.1	− 8.02 ± 0.60	LT
57059.06	5.20×10^{10}	205.3 ± 10.3	− 8.58 ± 0.27	LT
57375.22	4.30×10^{10}		− 9.06 ± 0.45	LT
57376.88	5.03×10^{10}	208.6 ± 13.6	− 9.27 ± 0.98	LT
57384.94	5.41×10^{10}	201.1 ± 13.3	− 9.48 ± 0.57	LT

Table A2. 4U 0115+63: EW(Hα) and ΔV measurements.

MJD	Radius (m)	ΔV (km s^{-1})	EW(Hα) (Å)	Telescope
47936	4.32×10^{10}		-9.36 ± 0.97	WHT
47936	4.93×10^{10}		-11.40 ± 1.19	WHT
48252	2.40×10^{10}	430.0 ± 14.8	-2.94 ± 0.89	INT
48252	2.78×10^{10}	400.0 ± 17.2	-2.89 ± 0.51	INT
48252	2.52×10^{10}	420.0 ± 16.0	-5.19 ± 0.37	INT
48252	2.78×10^{10}	400.0 ± 16.9	-4.81 ± 0.51	INT
48283	5.20×10^{10}		-12.33 ± 0.67	INT
48283	5.35×10^{10}		-12.89 ± 0.90	INT
48283	5.02×10^{10}		-11.72 ± 0.83	INT
48496	2.01×10^{10}	470.0 ± 7.9	-5.66 ± 0.48	INT
48604	1.85×10^{10}	490.0 ± 15.2	-6.71 ± 0.26	INT
48604	1.93×10^{10}	480.0 ± 20.6	-5.83 ± 0.28	INT
48839	2.52×10^{10}	420.0 ± 18.0	-4.37 ± 0.51	INT
48839	2.30×10^{10}	440.0 ± 22.6	-4.33 ± 0.79	INT
49005	2.30×10^{10}	440.0 ± 19.2	-7.77 ± 0.44	INT
49338	2.64×10^{10}	410.0 ± 16.5	-6.83 ± 0.76	WHT
49338	3.08×10^{10}	380.0 ± 18.2	-6.69 ± 0.92	WHT
49338	3.08×10^{10}	380.0 ± 15.1	-7.54 ± 0.57	WHT
49340	2.78×10^{10}	400.0 ± 17.6	-6.25 ± 0.34	WHT
49340	2.92×10^{10}	390.0 ± 17.3	-6.13 ± 0.59	WHT
49726	4.39×10^{10}		-9.57 ± 0.54	INT
49901	2.10×10^{10}	460.0 ± 7.0	-4.24 ± 0.21	INT
49901	2.20×10^{10}	450.0 ± 7.1	-5.45 ± 0.65	INT
49972	2.52×10^{10}	420.0 ± 8.2	-5.28 ± 0.23	INT
49972	2.64×10^{10}	410.0 ± 10.7	-5.34 ± 0.16	INT
50050	5.41×10^{10}		-13.10 ± 1.00	JKT
50094	7.72×10^{10}	240.0 ± 9.6	-12.81 ± 0.82	INT
50094	7.72×10^{10}	240.0 ± 13.9	-12.41 ± 0.90	INT
50094	7.72×10^{10}	240.0 ± 8.6	-11.86 ± 0.45	INT
50113	4.34×10^{10}	320.0 ± 8.3	-7.54 ± 0.30	INT
50113	4.34×10^{10}	320.0 ± 11.6	-8.61 ± 0.25	INT
50254	3.85×10^{10}	340.0 ± 11.7	-7.84 ± 0.94	INT
50273	2.52×10^{10}	420.0 ± 16.1	-6.61 ± 0.43	INT
50273	2.52×10^{10}	420.0 ± 13.4	-6.65 ± 0.55	INT
50480	2.01×10^{10}	470.0 ± 11.0	-4.34 ± 0.23	INT
51026	3.63×10^{10}	350.0 ± 10.3	-7.21 ± 1.22	INT
51066	3.85×10^{10}	340.0 ± 13.6	-7.43 ± 0.80	INT
51084	4.63×10^{10}	310.0 ± 12.4	-7.98 ± 0.51	INT
51175	4.89×10^{10}		-11.27 ± 0.57	INT
51385	5.51×10^{10}		-13.47 ± 0.57	Ski
51385	1.11×10^{11}	200.0 ± 8.7	-9.18 ± 0.20	Ski
51743	1.54×10^{11}	170.0 ± 10.2	-12.01 ± 0.15	Ski
51743	1.37×10^{11}	180.0 ± 12.6	-12.69 ± 0.34	Ski
51743	1.54×10^{11}	170.0 ± 11.1	-12.45 ± 0.31	Ski
51822	9.18×10^{10}	220.0 ± 19.4	-20.84 ± 0.65	Ski
51833	5.67×10^{10}	280.0 ± 9.7	-20.04 ± 0.91	Ski
52190	6.95×10^{9}	800.0 ± 20.1	-2.48 ± 0.23	Ski
52191	1.05×10^{10}	650.0 ± 14.5	-2.47 ± 0.91	Ski
52918	2.20×10^{10}	450.0 ± 10.0	-3.42 ± 0.34	Ski
53180	1.37×10^{11}	180.0 ± 12.0	-9.03 ± 0.65	Ski
53193	1.37×10^{11}	180.0 ± 11.2	-9.29 ± 0.37	Ski
53243	1.01×10^{11}	210.0 ± 17.6	-9.26 ± 0.56	Ski
53252	6.10×10^{10}	270.0 ± 9.8	-9.51 ± 0.59	Ski
53260	4.60×10^{10}		-10.13 ± 0.14	Ski
53261	5.29×10^{10}	290.0 ± 25.2	-9.27 ± 0.97	Ski
53303	5.84×10^{10}		-14.68 ± 0.45	Ski
53544	2.78×10^{10}	400.0 ± 17.6	-9.51 ± 0.97	Ski
53562	3.85×10^{10}	340.0 ± 9.8	-12.34 ± 0.92	Ski
53580	5.67×10^{10}	280.0 ± 11.8	-17.57 ± 0.23	Ski
53599	6.58×10^{10}	260.0 ± 13.6	-16.44 ± 0.44	Ski
53600	7.11×10^{10}	250.0 ± 14.9	-17.88 ± 0.64	Ski
53633	4.94×10^{10}	300.0 ± 13.5	-15.11 ± 0.89	Ski
53669	5.67×10^{10}	280.0 ± 17.2	-6.69 ± 0.55	Ski
54010	2.30×10^{10}	440.0 ± 28.8	-4.88 ± 0.46	Ski
54348	7.11×10^{10}	250.0 ± 12.5	-9.88 ± 0.76	Ski
54375	4.94×10^{10}	300.0 ± 13.1	-9.63 ± 0.90	Ski
54377	3.85×10^{10}	340.0 ± 13.7	-8.76 ± 0.92	Ski
54641	3.25×10^{10}	370.0 ± 20.4	-11.85 ± 0.94	Ski
54643	3.85×10^{10}	340.0 ± 13.9	-12.69 ± 0.93	Ski
54662	5.67×10^{10}		-14.07 ± 0.57	Ski
54686	2.40×10^{10}	430.0 ± 17.6	-12.92 ± 0.22	Ski
55041	8.57×10^{9}	720.0 ± 7.9	-1.46 ± 0.47	Ski
55220.86	1.37×10^{10}	570.0 ± 16.8	-4.25 ± 0.53	LT
55347.21	1.93×10^{10}	480.0 ± 16.9	-4.54 ± 0.91	LT
55361.13	2.64×10^{10}	410.0 ± 18.0	-5.79 ± 0.87	LT
55361.14	2.20×10^{10}	450.0 ± 15.9	-7.11 ± 0.23	LT
55361.15	3.08×10^{10}	380.0 ± 25.5	-8.15 ± 0.65	LT
55375.13	2.30×10^{10}	440.0 ± 18.0	-5.59 ± 0.89	LT
55375.14	2.40×10^{10}	430.0 ± 18.8	-6.76 ± 0.91	LT
55375.15	3.25×10^{10}	370.0 ± 8.1	-4.82 ± 0.67	LT
55403.21	4.43×10^{10}		-9.70 ± 0.47	LT
55403.21	4.28×10^{10}		-9.23 ± 0.59	LT
55403.22	4.11×10^{10}		-8.70 ± 0.34	LT
55410	4.71×10^{10}		-10.63 ± 0.51	LT
55435	4.63×10^{10}	310.0 ± 12.4	-6.61 ± 0.67	Ski
55437	4.08×10^{10}	330.0 ± 16.5	-7.14 ± 0.50	Ski
55453	3.85×10^{10}	340.0 ± 4.1	-7.24 ± 0.76	Ski
55469	3.64×10^{10}		-7.22 ± 0.33	Ski
55731.18	1.11×10^{11}	200.0 ± 9.8	-9.04 ± 0.54	LT
55738.20	4.64×10^{10}		-10.40 ± 0.65	LT
55751.17	3.08×10^{10}	380.0 ± 28.8	-9.12 ± 0.23	LT
55758.15	1.64×10^{10}	520.0 ± 12.5	-8.21 ± 0.56	LT
55793	5.29×10^{10}	290.0 ± 13.1	-13.13 ± 1.05	Ski
55801	5.67×10^{10}	280.0 ± 13.7	-13.18 ± 1.06	Ski
55812	2.52×10^{10}	420.0 ± 11.6	-14.60 ± 1.17	Ski
55812	2.52×10^{10}	420.0 ± 11.2	-19.89 ± 1.39	Ski
55834.99	5.75×10^{10}		-14.34 ± 1.29	LT
55841.99	5.97×10^{10}		-15.17 ± 1.27	LT
55897.84	4.63×10^{10}		-10.37 ± 0.90	LT
55904.90	3.39×10^{10}		-6.50 ± 0.52	LT
55925.84	4.62×10^{10}		-10.36 ± 0.89	LT
55941.98	5.23×10^{10}		-12.44 ± 0.74	LT
55946.90	4.73×10^{10}		-10.73 ± 0.97	LT
56084	2.20×10^{10}	450.0 ± 18.0	-3.87 ± 0.31	Ski
56163	1.05×10^{10}	650.0 ± 19.5	-2.22 ± 0.18	Ski
56183	1.09×10^{10}	640.0 ± 18.3	-1.58 ± 0.16	Ski
56466.13	2.99×10^{10}		-5.40 ± 0.43	LT
56472.13	2.20×10^{10}	450.0 ± 18.0	-5.50 ± 0.51	LT
56494.06	3.00×10^{10}		-5.42 ± 0.43	LT
56503	2.20×10^{10}	450.0 ± 28.4	-7.55 ± 0.76	Ski
56534	2.01×10^{10}	470.0 ± 4.7	-5.86 ± 0.87	Ski

Table A2 – *continued*

Table A3. V 0332+53: EW(Hα) and ΔV measurements.

MJD	Radius (m)	ΔV (km s^{-1})	EW(Hα) (Å)	Telescope
47919	1.70×10^{10}		-6.86 ± 0.58	INT
48136	1.51×10^{10}	150.0 ± 3.7	-7.63 ± 0.53	INT
48136	1.73×10^{10}	140.0 ± 10.9	-7.48 ± 0.67	INT
48136	1.73×10^{10}	140.0 ± 8.8	-6.69 ± 0.88	INT
48208	1.73×10^{10}	140.0 ± 10.4	-6.57 ± 0.25	INT
48209	1.80×10^{10}		-7.24 ± 0.34	INT
48209	2.00×10^{10}		-8.82 ± 0.21	INT
48209	1.70×10^{10}		-7 ± 0.89	INT
48209	1.70×10^{10}		-7.11 ± 0.80	INT
48252	1.80×10^{10}		-7.73 ± 0.33	INT
48252	2.00×10^{10}		-8.70 ± 0.79	INT
48252	2.40×10^{10}		-11.44 ± 0.93	INT
48283	1.90×10^{10}		-7.79 ± 0.45	INT
48283	1.80×10^{10}		-7.52 ± 0.90	INT
48496	1.51×10^{10}	150.0 ± 3.5	-5.45 ± 0.50	INT
48603	1.73×10^{10}	140.0 ± 7.0	-8.04 ± 0.67	INT
48604	1.33×10^{10}	160.0 ± 12.8	-5.24 ± 0.95	INT
48852	1.73×10^{10}	140.0 ± 9.1	-5.01 ± 0.23	INT
48939	1.60×10^{10}		-6.54 ± 0.76	INT
48939	1.18×10^{10}	170.0 ± 6.8	-4.23 ± 0.91	INT
48939	1.73×10^{10}	140.0 ± 7.4	-5.11 ± 0.34	INT
49326	1.73×10^{10}	140.0 ± 7.1	-10.06 ± 0.12	INT
51744	1.73×10^{10}	140.0 ± 12.0	-5.33 ± 0.81	Ski
51833	2.01×10^{10}	130.0 ± 10.4	-5.14 ± 0.57	Ski
51833	2.01×10^{10}	130.0 ± 4.2	-5.08 ± 0.57	Ski
52128	1.30×10^{10}		-4.65 ± 0.50	Ski
52128	1.20×10^{10}		-3.87 ± 0.33	Ski
52165	1.50×10^{10}		-5.90 ± 0.91	Ski
52918	1.20×10^{10}		-4.12 ± 0.73	Ski
53303	1.90×10^{10}		-8.16 ± 0.86	Ski
53580	1.40×10^{10}		-5.19 ± 0.23	Ski
53598	1.60×10^{10}		-6.29 ± 1.21	Ski
53633	1.40×10^{10}		-4.93 ± 0.80	Ski
53669	1.50×10^{10}		-5.55 ± 0.51	Ski
54350	1.40×10^{10}		-4.91 ± 0.41	Ski
54377	1.50×10^{10}		-5.81 ± 0.54	Ski
54686	1.60×10^{10}		-6.11 ± 0.21	Ski
54690	1.60×10^{10}		-6.38 ± 0.70	Ski
55102	1.60×10^{10}		-6.38 ± 0.23	Ski
55192.01	1.80×10^{10}		-7.66 ± 1.27	LT
55192.01	1.70×10^{10}		-6.98 ± 0.99	LT
55207.81	2.00×10^{10}		-8.90 ± 1.57	LT
55207.82	2.10×10^{10}		-9.27 ± 1.27	LT
55220.81	1.60×10^{10}		-6.24 ± 0.96	LT
55220.82	2.00×10^{10}		-9.05 ± 0.88	LT
55220.82	2.20×10^{10}		-9.79 ± 0.47	LT
55220.92	2.10×10^{10}		-9.39 ± 0.58	LT
55220.93	2.30×10^{10}		-10.60 ± 0.66	LT
55220.93	2.00×10^{10}		-8.71 ± 0.95	LT
55221.81	1.60×10^{10}		-6.38 ± 1.23	LT
55221.82	2.10×10^{10}		-9.48 ± 0.76	LT
55221.83	2.30×10^{10}		-10.55 ± 0.65	LT
55221.92	2.10×10^{10}		-9.76 ± 0.99	LT
55221.93	2.20×10^{10}		-10.08 ± 0.46	LT
55221.94	2.30×10^{10}		-10.48 ± 0.43	LT
55222.03	2.00×10^{10}		-9.08 ± 0.63	LT
55222.04	2.20×10^{10}		-10.35 ± 0.21	LT
55222.05	1.90×10^{10}		-8.34 ± 0.32	LT
55374.20	1.20×10^{10}		-4.19 ± 0.37	LT
55374.21	1.20×10^{10}		-4.08 ± 0.53	LT
55374.21	1.20×10^{10}		-4.09 ± 0.59	LT
55402.12	8.10×10^{09}		-2.28 ± 0.76	LT
55402.13	7.10×10^{09}		-1.86 ± 0.70	LT
55402.14	8.60×10^{09}		-2.48 ± 0.73	LT
55411	1.30×10^{10}		-4.82 ± 0.27	Ski
55436	1.40×10^{10}		-5.07 ± 0.11	Ski
55453	1.60×10^{10}		-6.19 ± 0.23	Ski
55469	1.50×10^{10}		-5.66 ± 0.56	Ski
55794	1.70×10^{10}		-6.65 ± 0.87	Ski
55810	2.20×10^{10}		-10.13 ± 0.27	Ski
56164	1.60×10^{10}		-6.12 ± 0.12	Ski
56184	1.70×10^{10}		-6.68 ± 0.65	Ski
56535	1.50×10^{10}		-5.79 ± 0.31	Ski
56584	1.80×10^{10}		-7.23 ± 0.40	Ski

Table A3 – *continued*

Table A4. EXO 2030+375: EW(Hα) and ΔV measurements.

MJD	Radius (m)	ΔV (km s^{-1})	EW(Hα) (Å)	Telescope
46680	1.71×10^{11}		-15 ± 0.95	INT
48897	2.56×10^{11}		-27.32 ± 1.78	WHT
48898	2.32×10^{11}		-23.62 ± 1.54	WHT
48898	2.33×10^{11}		-23.75 ± 1.54	WHT
49166	1.84×10^{11}		-16.77 ± 1.00	WHT
49166	1.97×10^{11}		-18.54 ± 1.21	WHT
49166	1.92×10^{11}		-17.78 ± 1.16	WHT
49167	1.71×10^{11}		-15.04 ± 0.98	WHT
49167	1.62×10^{11}		-13.80 ± 0.90	WHT
49167	1.91×10^{11}		-17.68 ± 1.15	WHT
49167	2.15×10^{11}		-21.05 ± 1.37	WHT
49167	1.95×10^{11}		-18.27 ± 1.19	WHT
49167	1.85×10^{11}		-16.85 ± 1.10	WHT
49167	1.84×10^{11}		-16.72 ± 1.09	WHT
49167	1.96×10^{11}		-18.41 ± 1.20	WHT
49167	2.09×10^{11}		-20.27 ± 0.70	WHT
49167	2.15×10^{11}		-21.09 ± 1.37	WHT
49167	2.06×10^{11}		-19.74 ± 1.10	WHT
49167	2.22×10^{11}		-22.14 ± 0.9	WHT
49168	1.65×10^{11}		-14.21 ± 0.67	WHT
49168	1.67×10^{11}		-14.45 ± 1.17	WHT
49168	2.02×10^{11}		-19.20 ± 1.29	WHT
49168	2.08×10^{11}		-20.09 ± 1.21	WHT
49168	1.76×10^{11}		-15.59 ± 0.64	WHT
49168	1.86×10^{11}		-16.96 ± 0.52	WHT
49168	1.94×10^{11}		-18.09 ± 0.78	WHT
49168	2.07×10^{11}		-19.90 ± 0.77	WHT
49168	1.98×10^{11}		-18.64 ± 1.21	WHT
50272	1.30×10^{11}		-9.88 ± 1.30	WHT
50273	1.20×10^{11}		-8.80 ± 0.87	WHT
50273	1.50×10^{11}		-12.29 ± 1.43	WHT
50273	1.48×10^{11}		-12.11 ± 1.90	WHT
54004	1.19×10^{11}		-8.70 ± 0.70	RT
54093	1.21×10^{11}		-8.90 ± 0.71	RT
54356	1.32×10^{11}		-10.20 ± 0.82	RT

Table A5. 1A 1118−61: EW(Hα) and ΔV measurements.

MJD	Radius (m)	ΔV (m s^{-1})	EW(Hα) (Å)	Telescope
49049	8.92×10^{10}		-64.54 ± 3.58	SAAO
49050	9.36×10^{10}		-69.27 ± 2.91	SAAO
49160	9.25×10^{10}		-68.10 ± 0.97	SAAO
49161	8.35×10^{10}		-58.41 ± 3.83	SAAO
49418	8.71×10^{10}		-62.28 ± 3.21	SAAO
49535	8.62×10^{10}		-61.32 ± 1.98	SAAO
49536	8.64×10^{10}		-61.53 ± 3.91	SAAO
49773	9.16×10^{10}		-67.06 ± 2.17	SAAO
50176	8.77×10^{10}		-62.84 ± 2.73	SAAO
50619	9.54×10^{10}		-71.29 ± 0.95	SAAO
50849	8.68×10^{10}		-61.88 ± 2.47	SAAO
51187	8.63×10^{10}		-61.39 ± 2.54	SAAO
53444	9.05×10^{10}		-65.95 ± 2.51	SAAO
53448	9.31×10^{10}		-68.73 ± 3.31	SAAO
54226	9.01×10^{10}		-65.42 ± 3.67	SAAO
56317.46	8.75×10^{10}		-62.69 ± 2.92	SALT
56350.60	8.66×10^{10}		-61.73 ± 2.66	SALT

This paper has been typeset from a TEX/LATEX file prepared by the author.